Supporting Information

Noninvasive *In Situ* NMR Study of "Dead Lithium" Formation and Lithium Corrosion in Full-Cell Lithium Metal Batteries

Anna B. Gunnarsdóttir,[1] Chibueze V. Amanchukwu,[1,2,3] Svetlana Menkin,[1] and Clare P. Grey[1]*

1. Department of Chemistry, University of Cambridge, Cambridge, CB2 1EW, U.K.
2. Department of Chemical Engineering, Stanford University, Stanford, California 94305, United States
3. Present address: Pritzker School of Molecular Engineering, University of Chicago, Chicago, Illinois 60637, United States

*Corresponding author: cpg27@cam.ac.uk

Contents

The skin depth of Li metal in the NMR experiments

The application of the excitation rf-pulse in NMR spectroscopy, generates a B_1-field perpendicular to the static B_0-field. This causes a rotation of the net nuclear magnetization about the B_1 axis where the flip angle depends on the duration and the amplitude of the rf pulse. For non-metallic samples that do not experience skin effects, the nutation of the nuclear magnetization results in a sinusoidal curve for the signal intensity with the highest signal intensity is observed for a flip angle of 90°. For metallic samples however, due to skin depth effects, the rf field varies as a function of distance in the sample and the corresponding flip angle varies at different depths from the metal surface.[1–3]

For a radiofrequency (rf) field of strength ω_1, the field inside a metal is given by:[1]

$$\omega_1(x) = \omega_1(0)e^{-\frac{x}{d}} \qquad \text{Equation S1}$$

where d is the skin depth of the metal at frequency ν:[4]

$$d = \sqrt{\frac{\rho}{\pi \mu_0 \mu_r \nu}} \qquad \text{Equation S2}$$

and ρ the resistivity of the metal (94.7 n Ω for Li metal at 298 K), μ_0 is the permeability of the vacuum ($4\pi\ 10^{-7}$ m kg/ s^2A^2), μ_r is the relative permeability of the medium (μ_r = 1.4 for Li metal) and ν is the frequency of the applied rf field.[5] The resonance frequency for ^{7}Li in this study is 116.7 MHz, which results in a skin depth of 12.1 μm.

The skin depth effect leads to a more complex nutation behaviour of metals with the maximum signal intensity obtained at a flip angle of about ~133°.[1,3] A nutation experiment was performed at the end of plating Li metal on Cu (with plating capacity of 1 mAh/cm^2) to inspect whether skin depth effects were observed for the Li deposits. A sinusoidal nutation curve is observed for the Li deposits (Figure S1), the corresponding 90° pulse for a pulse duration of 5.5 μs. In contrast the highest intensity for the Li metal foil is at ~8.1 μs. This indicates that the NMR measurements of the Li deposits are not affected by skin depth effects and the deposits are less than 12 μm in width.[6] Furthermore, the linear increase in intensity observed on plating (Figure 2b, main text) is consistent with a quantitative excitation.

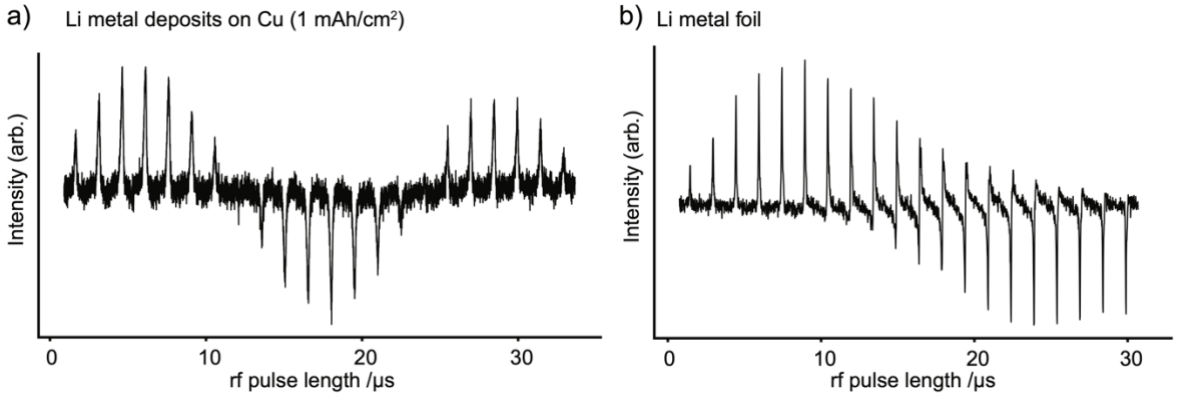

Figure S1. Experimental nutation curves of **a)** the Li deposits on Cu (1 mAh/cm^2) nutate sinusoidally as expected for samples that do not experience skin depth issues. **b)** The pristine Li metal foil nutates in a more complex way due to to skin depth effects.

Calculation of the SEI capacity

The SEI capacity on the first cycle, here used to define the capacity lost to all electrochemical and irreversible side reactions, can be estimated from the dead Li_{NMR} measured by NMR and the Coulombic efficiency (CE) from the electrochemistry. The CE is calculated as follows:

$$\mathrm{CE} = \frac{\mathrm{C_{stripping}}}{\mathrm{C_{plating}}} \qquad \text{Equation S3}$$

Where C_{plating} is the full plating capacity, assuming no side reactions ($C_{\mathrm{plating}} = 1$ mAh/cm^2 here). The capacity loss (CL) in cycle n is defined as:

$$\mathrm{CL} = \mathrm{C_{plating}} - \mathrm{C_{stripping}} \qquad \text{Equation S4}$$

CL is a combination of the capacity lost due to dead Li formation and the electrochemical formation of the SEI:

$$\mathrm{CL_n} = C_{dead\ Li,n} + C_{SEI,n} \qquad \text{Equation S5}$$

where the $C_{dead\ Li}$ is the capacity loss due to dead Li formation in cycle number n and C_{SEI} the SEI capacity corresponding to the current passed to form the SEI electrochemically on each cycle.

We first normalised all the NMR measurements (i.e., the Li metal signal intensity) to that observed in the first cycle, setting its value at the end of plating as 1. We then define a parameter, $\chi_{dead\ Li_{NMR}}$, as the normalised intensity at the end of discharge, that is the ratio of the intensity of the Li metal at the end of the discharge to that measured at the end of the 1st charge. This is simply the intensity at the end of each cycle (e.g. shown in Figure 2b) due to our normalisation.

In order to extract capacities from the NMR observed intensities we need to account for the SEI formation in the 1st charge, $C_{SEI,n=1}$, i.e.,

$$\mathrm{C_{plating}}(1\ \mathrm{mAh/cm^2}) = C_{Li_{NMR},1} + C_{SEI,1} \qquad \text{Equation S6}$$

Where $C_{Li_{NMR},1}$ is the capacity observed by NMR (and effectively used to normalise the subsequent NMR measurements). Thus, the capacity corresponding to the dead Li, $C_{dead\ Li}$ is simply given by

$\chi_{dead\ Li_{NMR}} \times C_{Li_{NMR},1}$, which can be solved to give:

$$C_{dead\ Li} = \left(C_{\mathrm{plating}} - C_{SEI,1}\right) \times \chi_{dead\ Li_{NMR}} \qquad \text{Equation S7}$$

Equation S5 can now be rewritten as:

$$\mathrm{CL_n} = \left(C_{\mathrm{plating}} - C_{SEI,1}\right) \times \chi_{dead\ Li_{NMR},n} + C_{SEI,n} \qquad \text{Equation S8}$$

This calculation neglects Li corrosion, which is expected to continue throughout.

We now evaluate the role of corrosion. The capacity loss is still described by Equation S5, because the corrosion current does not result in net current in the circuit. The capacity ascribed to the observed NMR signal, however, $\mathrm{C_{Li_{NMR},1}}$, does depends on both corrosion capacity and SEI capacity:

$$\mathrm{C_{Li_{NMR},1}} = \mathrm{C_{plating}}\left(1\,\frac{\mathrm{mAh}}{\mathrm{cm^2}}\right) - \mathrm{C_{SEI,1}} - \mathrm{C_{corrosion}} \qquad \text{Equation S9}$$

and Equation S5 becomes:

$$\mathrm{CL_n} = \left(C_{\mathrm{plating}} - C_{SEI,1} - C_{corrosion}\right) \times \chi_{dead\ Li_{NMR},n} + C_{SEI,n} \qquad \text{Equation S10}$$

which yields an equation with two unknowns, the SEI capacity and the corrosion capacity.

The corrosion capacity in LP30 may be estimated from the corrosion current, 29 µA/cm^2 (Table 2, main text). Thus, the corrosion capacity during two hours of plating could be as high as 58 µAh/cm^2. Performing the same analysis as before on the data presented in Figure 2. The $\mathrm{CL_{n=1}}$ on first cycle is 0.17 mAh/cm^2, $\mathrm{C_{corrosion}}$ = 0.06 mAh/cm^2 and the dead $\mathrm{Li_{NMR}}$ value is 0.08. This results in similar values; the SEI capacity of changing from 0.098 to 0.10 mAh/cm^2 and dead Li value of 0.07 mAh/cm^2.

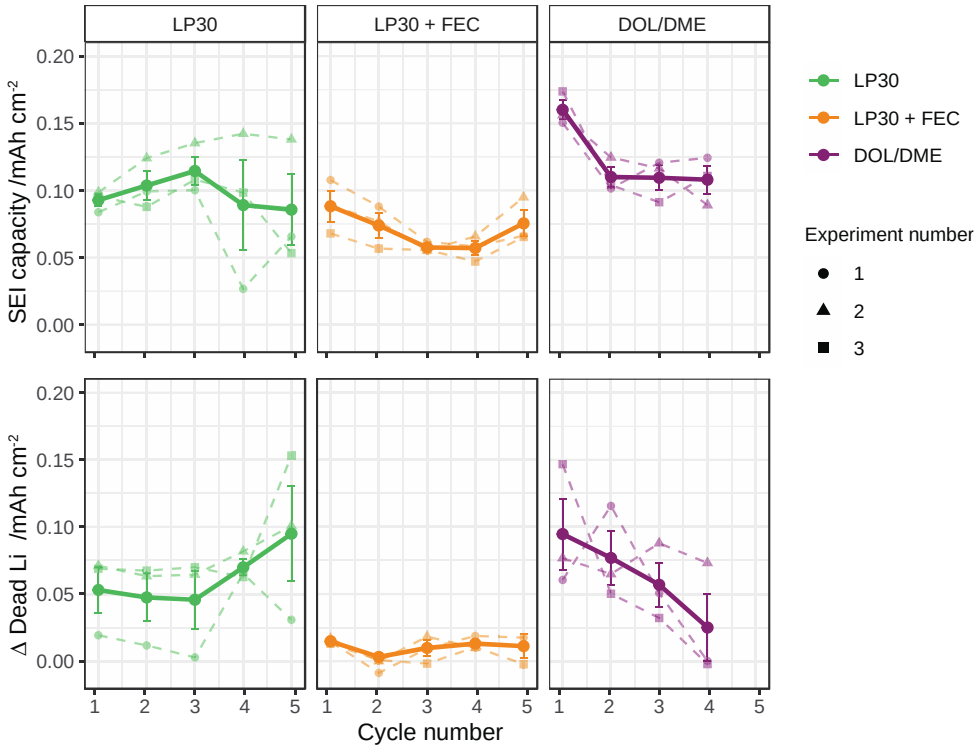

Figure S2. The average SEI formation capacity (top) and dead Li (bottom) per cycle, in LP30, LP30 + FEC and DOL/DME. The dashed lines show the values used to calculate the mean and the standard deviation, for the three different sets of *in situ* NMR experiments.

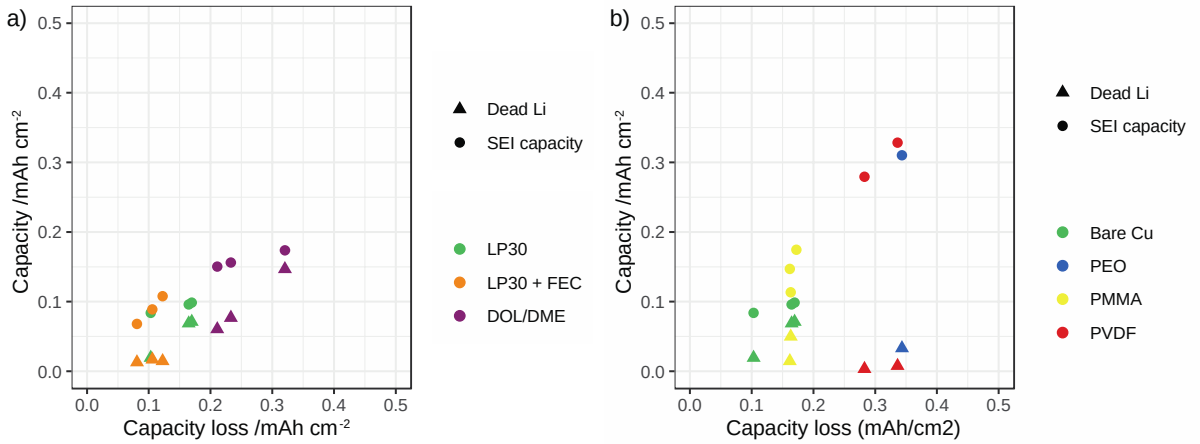

Figure S3. Capacity losses in the first cycle, the SEI capacity C_{SEI} (triangles) and the dead Li capacity $C_{dead\ Li}$ (circles) plotted against the corresponding capacity loss, CL. **a)** In the three electrolytes, LP30, LP30 + FEC and DOL/DME on bare Cu current collector, same data is shown Figure 3e and 3f in the main text. The different data points corresponds to different sets of *in situ* experiments. **b)** In LP30 on bare Cu (green) and on polymer-coated Cu (PEO, PMMA and PVDF) calculated from the data presented in Figure 5 in the main text. Greater SEI capacity is observed for the polymer-coated Cu cells and less dead Li formation.

Corrosion

Long term Li metal dissolution

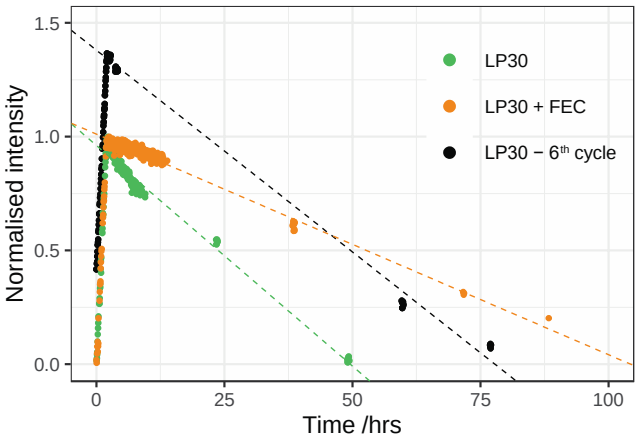

Figure S4. The long-term corrosion behavior was probed by *ex situ* NMR measurements. After the *in situ* measurements, the cell was transported back into a glovebox were it rested at the OCV and was taken out and put into the magnet to be measured ex situ at various time intervals. In black is the corrosion of Li metal at the top of charge for the 6th deposition, normalized to the first cycle intensity, for the cell shown in Figure 2b. The dashed line represents the linear fit through the data points to guide the eye.

Li corrosion followed by Li stripping

Figure S5 shows the corrosion experiment for DOL/DME (the dissolution curve also shown in Figure 6b) and LP30 (using 0.02 mA/cm^2 SEI formation current) where after about 18 hrs of rest at the OCV, the lithium was completely stripped off using 0.5 mA/cm^2. Interestingly, for DOL/DME the amount of dead Li after stripping (Figure S5) is less for the corrosion experiment compared to stripping without the rest period; that is a dead Li of around 5% of the plating capacity compared to on average of 11% without the rest period (Table 1). For LP30, the dead Li_{NMR} after stripping is on average 6% (Table 1), which is the same as measured after stripping with the rest period (Figure S5).

This indicates that the corrosion of Li metal, as measured here by NMR, does not result in a significant formation of dead Li prior to stripping by a loss of contact to the Cu electrode. Furthermore, the small amount of dead Li_{NMR} left in the cell after stripping does not dissolve further (stable intensity seen after stripping at ~21-24 hours).

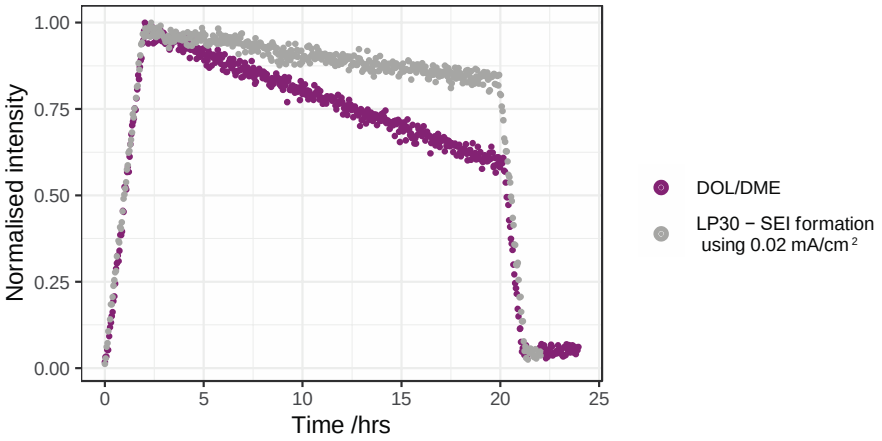

Figure S5. ***In situ*** **NMR measurements of the corrosion followed by stripping** The normalised integrated intensity of the Li metal intensity during the first 2 hours of deposition using 0.5 mA/cm^2 (corresponding to 1 mAh/cm^2) and the corresponding decrease during the OCV period of roughly 18 hours followed by stripping at 0.5 mA/cm^2 in DOL/DME (purple) and LP30 with the initial SEI formation on Cu using 0.02 mA/cm^2 (compared to 0.5 mA/cm^2 used in all experiments where it is not stated specifically, gray). The formation period on Cu using 0.02 mA/cm^2 before plating is not shown, as there is no Li metal signal to integrate. Thus, time = 0 hrs equals the time at the start of Li plating.

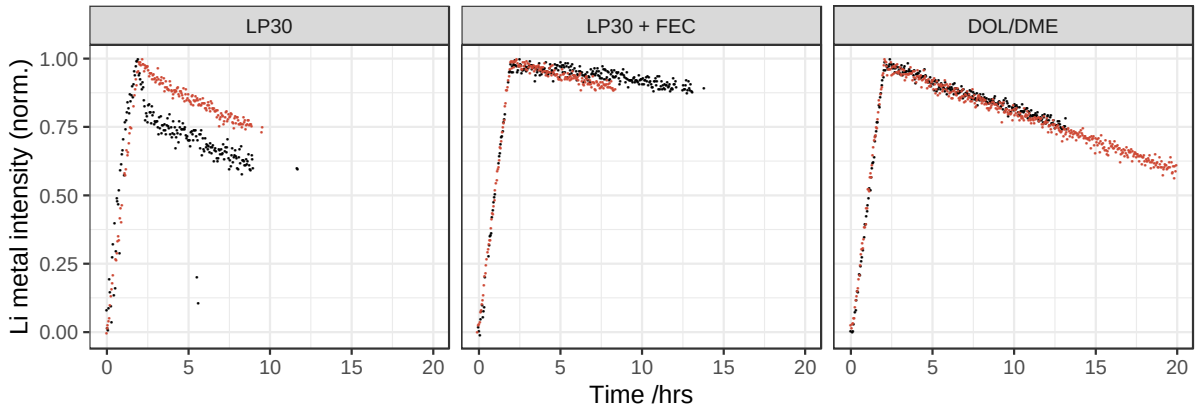

Figure S6. ***In situ*** **corrosion experiments** The integrated intensity of the Li metal intensity during the first 2 hours of deposition using 0.5 mA/cm^2 (corresponding to 1 mAh/cm^2) and the corresponding decrease during the OCV period for two sets of experiments in LP30, LP30 + FEC and DOL/DME.

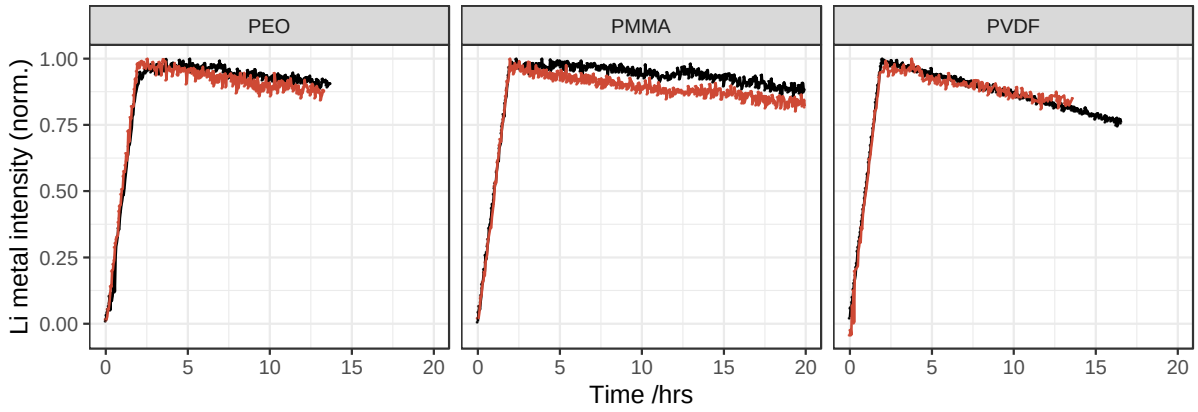

Figure S7. ***In situ*** **corrosion experiments with polymer-coated Cu** The integrated intensity of the Li metal intensity during the first 2 hours of deposition using 0.5 mA/cm^2 (corresponding to 1 mAh/cm^2) and the corresponding decrease during the OCV period for two sets of experiments in LP30 with PEO-, PMMA- and PVDF-coated Cu.

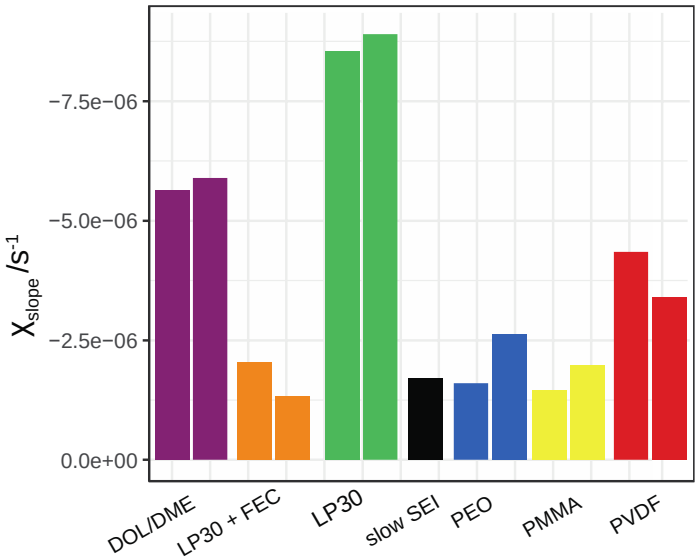

Figure S8. A bar chart showing the slope of the dissolution curve ($\boldsymbol{\chi_{slope}}$ /s^{-1}) from a linear fit to the different sets of *in situ* NMR measurements in different electrolytes and with different polymer coatings.

Table S1. The corrosion current calculated assuming 100% current efficiency (i.e. no electrochemical SEI formation the current density becomes $\boldsymbol{i_{corr} = C_{plating} \times \chi_{slope}}$), in contrast to the values reported in Table 2 that take into account the SEI capacity calculated from the *in situ* NMR measurements.

Electrolyte/ Polymer coating	χ_{slope} /s^{-1}	i_{corr} /μA cm^{-2}
LP30	-8.7	31
LP30 – 6th cycle	-9.6	35
LP30–slow SEI formation	-1.7	6.2
LP30 + FEC	-1.7	6.1
DOL/DME	-5.8	21
PEO-coating	-2.1	7.6
PMMA-coating	-1.7	6.2
PVDF-coating	-3.9	14

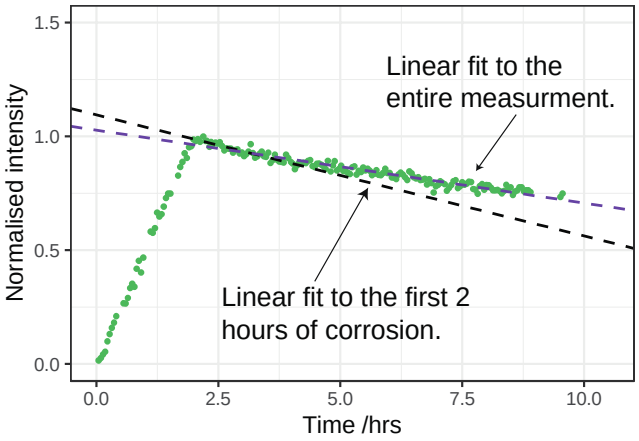

Figure S9. The corrosion of Li metal on bare Cu in LP30, also shown in Figure 6 in the main text. The dashed lines show the linear fit obtained when accounting for only the first two hours of rest at OCV compared to for the entire measurement. The corrosion current, i_{corr} for the first two hours is 49 μA cm^{-2}. Averaging over the whole measurement results in 28 μA cm^{-2}.

Bulk magnetic susceptibility effects

^{7}Li shift of the pristine Li metal

To understand the shifts observed in the *in situ* Cu-LFP cells, the effect of the paramagnetic LFP cathode on the Li metal shift is first studied in a pristine Li-LFP cell. The Li metal peak of a pristine Li-Li cell (when the electrodes are oriented perpendicular to the static, applied magnetic field) appears at 244 ppm (Figure S10, black) and when paired with the LFP cathode, the Li metal peak shifts to 260 ppm (Figure S10, purple). A paramagnetic material can cause both a shift and significant broadening of NMR resonances due to bulk magnetic susceptibility effects.[7] Previously, the resonance of Li metal has been shown to shift significantly when assembled with the paramagnetic spinel cathode, $Li_{1.08}Mn_{1.92}O_4$, from 245 ppm to 368 ppm (and with additional asymmetric broadening of the metal peak).[7] In a Li-Cu cell, there is no significant shift in the ^{7}Li metal peak (Figure S10, red). The magnetic susceptibility of Cu metal is negative (the diamagnetic contribution being larger than the paramagnetic contribution, $\chi_{Cu,volume} = -9.63 \times 10^{-6}$)[8]. In conclusion, we can expect that the ^{7}Li metal peak in Cu-LFP cells will have a higher shift than what is typically observed in Li-Li cells.

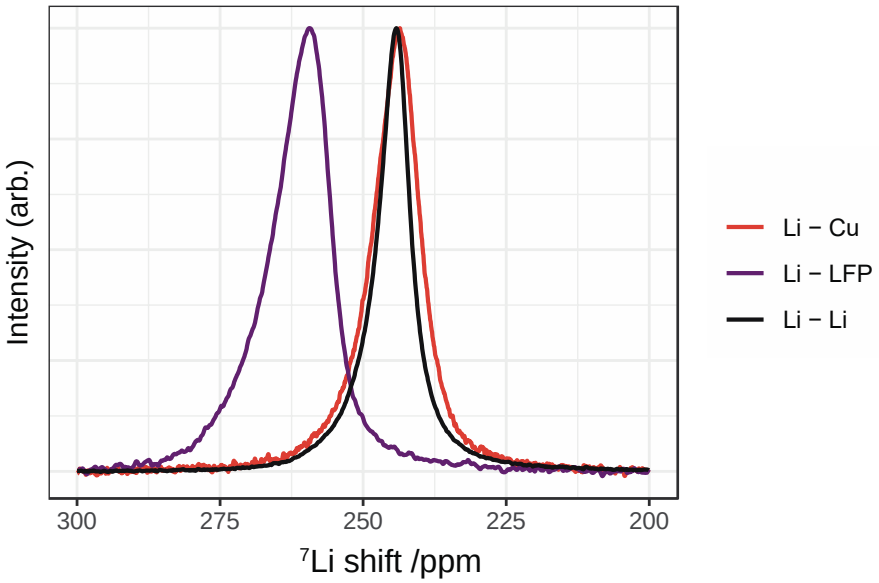

Figure S10. **BMS effects on the pristine Li metal resonance**: ^{7}Li NMR spectra of pristine Li metal oriented perpendicular to the magnetic field in three different configurations; Li-Cu cell (red), Li-LFP cell (purple) and Li-Li cell (black). The ^{7}Li shift of Li metal when assembled against the paramagnetic LFP cathode shifts from 245 ppm to 260 ppm due to BMS effects. The main plane of the rectangular electrode is facing perpendicular with respect to the applied magnetic field B_0, that is at 90°.

Susceptibility calculations of ^{7}Li metal shifts

Susceptibility calculations were used to understand the observed shifts of the Li electrodeposits on the electrode surface of both Li and Cu. The calculations were performed using a simulation code previously published in reference [3]. The code was then modified to fit the experimental setup presented here, simulating Li deposits on a Cu electrode.

The method takes a 3D grid as an input that represents the macroscopic structure that needs simulating, where the grid contains the susceptibility values representing each material in the model. A 3D Fourier transform (using the fast Fourier transform (FFT) method[9,10]) is taken of the susceptibility distribution to calculate any modifications to the magnetic field at each position.[3,11] The susceptibility-corrected field-map is then used to calculate the shift at each point in the cell and an NMR spectrum created by representing the shift distribution in a histogram as described in previous work.[3]

The Knight shift of metals must be accounted for when calculating the shift of Li metal. The Knight shift results in a constant offset that scales directly with the resonance frequency, $\Delta B = -KB_0$ and $K = 0.0261\%$ for ^{7}Li metal.[4,12] Thus, an additional shift of 261 ppm is added to the local susceptibility-corrected magnetic field of Li metal.[3]

An array of 256^3 points was used for the input grid, representing a cubic cell with 12.75 mm sides and each point in the array corresponding to a 50 μm^3 voxel. A pristine Li or Cu electrode was represented by a rectangular electrode in the middle of the cubic array, with sides 4.0 × 10.0 × 0.4 mm in x, y and z directions. The applied magnetic field, $\boldsymbol{B_0}$ is aligned along z direction matching the geometry of the NMR experiment. The voxels inside the rectangular electrode were either assigned a volume susceptibly of either $\chi_{Cu,vol}$ or $\chi_{Li,vol}$. The susceptibility values used are in SI units and are: $\chi_{Cu,vol} = -9.63 \times 10^{-6}$,[8] $\chi_{Li,vol} = 24.5 \times 10^{-6}$ and the rest of the cell is modelled as a vacuum with $\chi_{vol} = 0$.[3] The formation of the microstructures was modelled by assigning single voxels at random points next to the rectangular electrode surface with a susceptibility value of $\chi_{Li,vol}$ following the approach of Ilott et al. The surface coverage of the voxels was varied from 2.5-95% [11]

In previous work by Ilott et al. the Li microstructures were represented by a single voxel randomly placed on the electrode surface with the surface coverage set to 20%, which results in a shift of 261 ppm (Figure S11a).[11] In the same study, Li dendrites were simulated by creating 1×1×8 voxels randomly placed perpendicular to the electrode's surface (as shown in the inset, Figure S11b) and the surface coverage set to 2.5% (for them to occupy the same volume as in the simulation of microstructures).[11] This results in a shift of 270 ppm for Li dendrites (Figure S11b) as a result of the BMS effects of Li metal and agrees well with the experimental observations by Chandrashekar et al.[1,11,13] To extend this study further, here the surface coverage of the microstructures (single voxels) was increased to 50% (Figure S11c). The microstructure peak now shifts to 256 ppm, indicating that due to BMS effects, higher surface coverages of Li deposits move to lower shifts, starting to resemble more the bulk Li metal at 245 ppm.

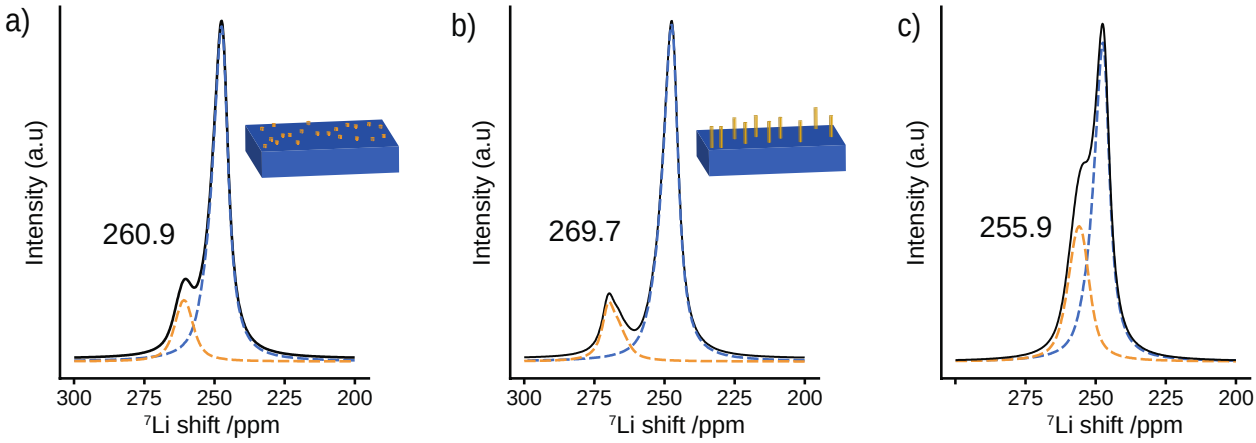

Figure S11. Simulated NMR spectrum of electrodeposits on Li metal from the susceptibility calculations of a pristine Li metal (in blue) and Li electrodeposits (in orange), the sum of the two shown in black. **a)** The simulated NMR spectrum with 20% coverage of Li microstructures (each microstructure is represented in a single voxel as illustrates in the inset) and **b)** of Li dendrites with 2.5% coverage (each dendrite is represented in 1× 1× 8 voxels as illustrated in the inset), which reproduces the results found in reference [11] with the shift of mossy microstructures at around 260 ppm and around 270 ppm for dendrites. **c)**The simulated NMR spectrum with a microstructure coverage of 50%. The shift is at 256 ppm for the microstructure peak (in orange).

Taking this approach further, the microstructure surface coverage (randomly placed voxels on the electrode surface) was varied between 2.5-95% on both Li metal and Cu foil (Figure S12). The overall trend is that a higher surface coverage leads to a lower shift due to BMS effects (Figure S12b). A shift to lower resonances correlates well with what is seen experimentally in the Cu-LFP cells (Figure 4,

Figure S13 and Figure S14), where a gradual shift in the Li metal peak occurs during plating indicating a higher coverage of deposits. Due to the susceptibility of Li metal being slightly paramagnetic ($\chi_{Cu,vol} = -9.63 \times 10^{-6}$,[8] $\chi_{Li,vol} = 24.5 \times 10^{-6}$ in SI units), the calculated values are at a slightly lower shift compared to when simulated on Cu.

In practice, the shift is influenced by all the components of the cell and the shifts observed experimentally (the initial peak emerging at 273 ppm in Cu-LFP cells) are not be directly comparable to the calculations (that gives 260 ppm on Cu for the lowest surface coverage). The higher shift observed experimentally is consistent with the higher shift of Li metal foil when assembled with the paramagnetic LFP cathode, as shown in Figure S10 (about 15 ppm shift). It is important to note that the single voxels used in the susceptibility simulations to represent Li microstructures is a crude simplification of Li morphology. The Li microstructures are likely to grow further away from the electrode, which results in a higher observed shift as shown for the simulation of dendrites (Figure S11b). Thus, any estimation of surface coverage based on the shift will probably lead to an underestimation as other factors in the morphology (such as Li growing away from the electrode surface) lead to higher observed metal shifts.

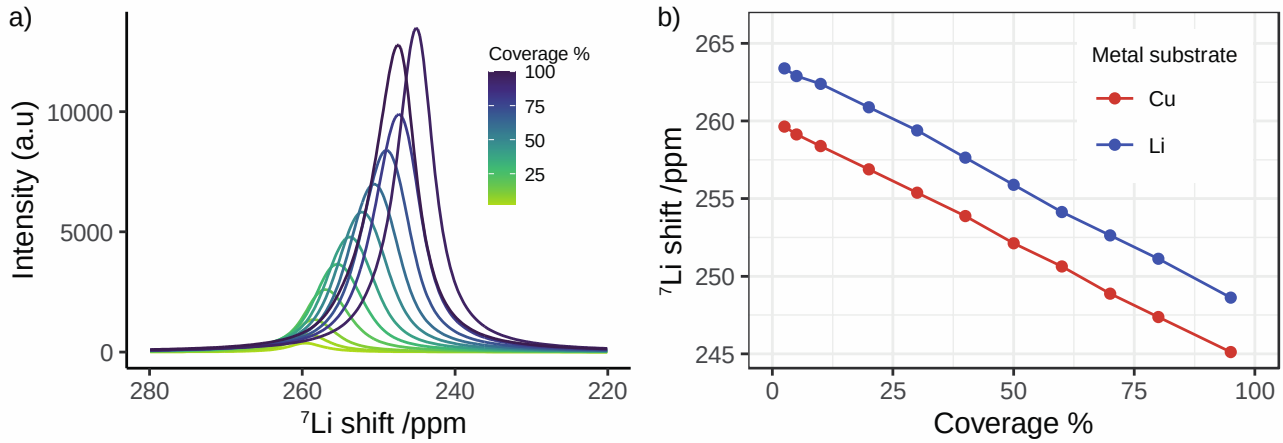

Figure S12. The Li metal shift as a function of surface coverage of Li microstructures. **a)** The simulated NMR spectra of the microstructure deposits on Cu, varying the surface coverage from 2.5-95%. **b)** The ^{7}Li metal shift at the peak maxima of the Li microstructure peak on a Cu (red) or Li metal (blue) electrode. The calculated shift at 2.5% surface coverage is 260 ppm on Cu and 263 ppm on Li.

^{7}Li shift of Li deposits in Cu-LFP cells

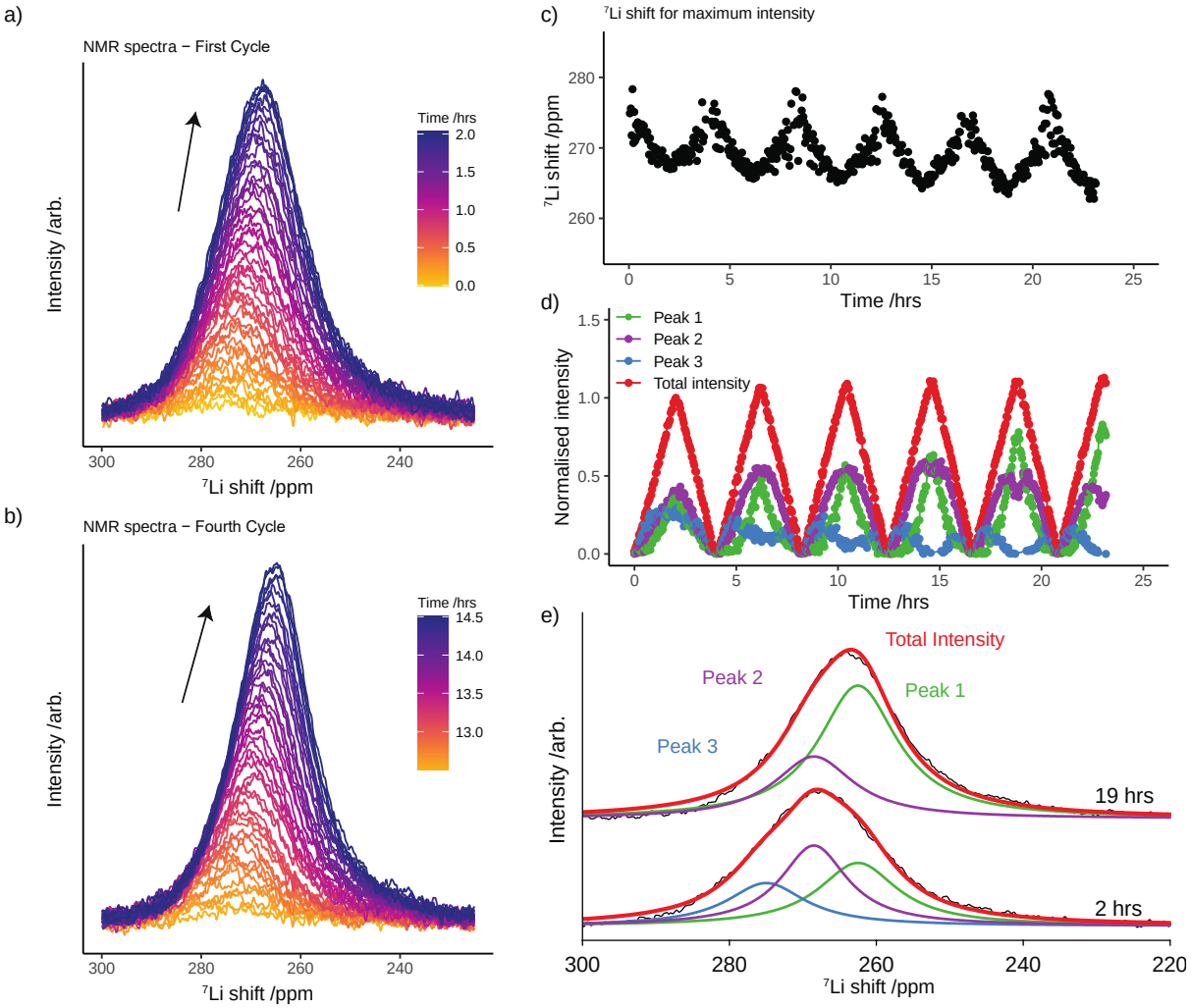

Figure S13. ^{7}Li metal shift in LP30 + FEC electrolyte. **a)** The Li metal spectra during charge (plating) in the first cycle. **b)** The Li metal spectra during charge (plating) in the fourth cycle. **c)** The ^{7}Li shift of the maximum intensity of the Li metal resonance during cycling. **d)** The deconvoluted intensities of the Li metal spectra during cycling. **e)** An example of the fitted spectra at the end of charge in first and fifth cycle.

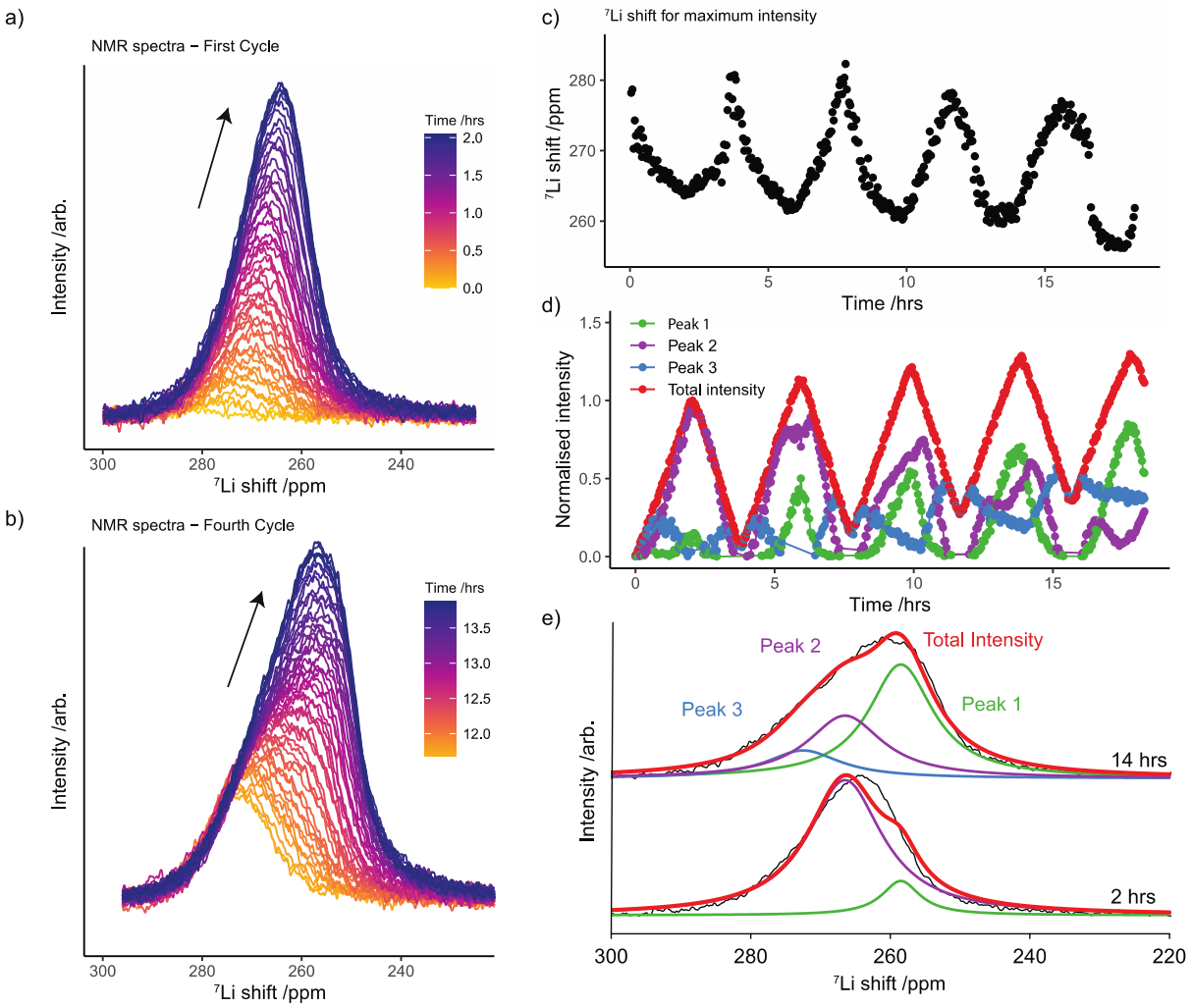

Figure S14. ^{7}Li metal shift in in DOL/DME electrolyte. **a)** The Li metal spectra during charge (plating) in the first cycle. **b)** The Li metal spectra during charge (plating) in the fourth cycle. **c)** The ^{7}Li shift of the maximum intensity of the Li metal resonance during cycling. **d)** The deconvoluted intensities of the Li metal spectra during cycling. **e)** An example of the fitted spectra at the end of charge in first and fourth cycle.

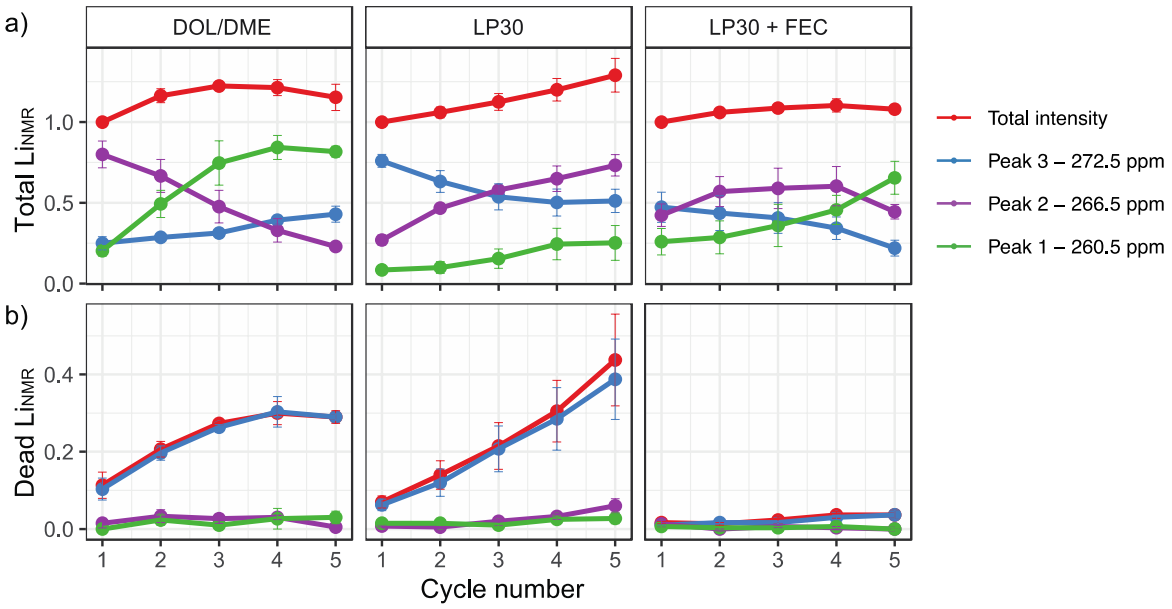

Figure S15. The normalised intensity of the deconvoluted peaks at **a)** the end of charge (plating, after depositing 1 mAh/cm^2 of Li metal) and **b)** at the end of discharge (stripping) in the three electrolytes. Peak 1, at the lowest ^{7}Li metal shift, increases in intensity between cycles for all electrolytes during plating and is most apparent in the DOL/DME electrolyte. The dead Li peak measured in DOL/DME and LP30 is fully captured by Peak 3, at the highest ^{7}Li metal shift.

Deconvolution of Li metal shifts on polymer-coated Cu

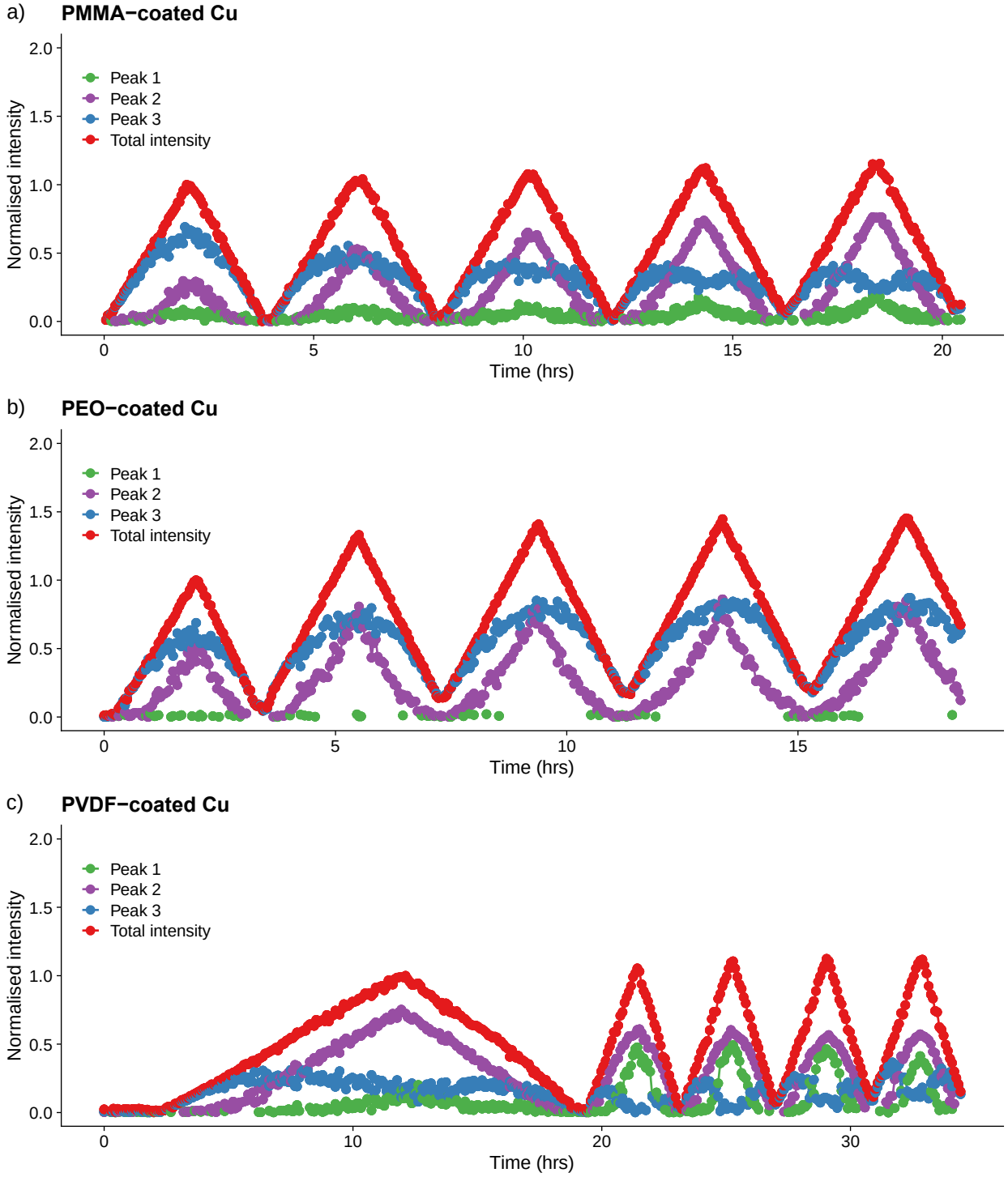

Figure S16 The ^{7}Li shift of Li metal peak on the polymer-coated Cu in LP30 electrolyte for **a)** PMMA-coated, **b)** PEO-coated and **c)** PVDF-coated Cu in LP30 electrolyte during plating and stripping, deconvoluted by three peaks at 260.5 ppm (Peak 1), 268.5 ppm (Peak 2) and 272.5 ppm (Peak 3). Note that the first plating and stripping cycle on PVDF-coated Cu was performed at 0.1 mA/cm^2 and the subsequent cycles at 0.5 mA/cm^2. The lower current density of 0.1 mA/cm^2 for PVDF was originally chosen as a pre-cycling step to limit the influence of ionic resistance at the polymer/Cu interface, the PVDF coating will swell only slightly in the electrolyte.[14] The lower current density likely leads to more homogeneous initial deposition, as seen for the Li metal, which has a lower shift (at 265.6 ppm) and greater contribution from Peak 2 compared to PEO and PMMA (at 270-271 ppm). This implies a more homogeneous surface coverage of Li deposits likely due to the lower current density used on first cycle. Although the first cycle for PVDF was performed at a lower current of 0.1 mA/cm^2 subsequent deposition at 0.5 mA/cm^2 (the current used for the other two systems in all cycles) showed continuing shift to lower ppm values (262 ppm) likely due to initial smooth deposition with the low current on first cycle. For the corrosion experiments the Li was deposited

at 0.5 mA/cm^2 for all the polymer coatings and now a higher shift is observed for the PVDF system (at 271 ppm), closer to that of the PMMA and PEO systems – showing that current is an important factor in controlling homogeneity of the coatings.

Electrochemistry data

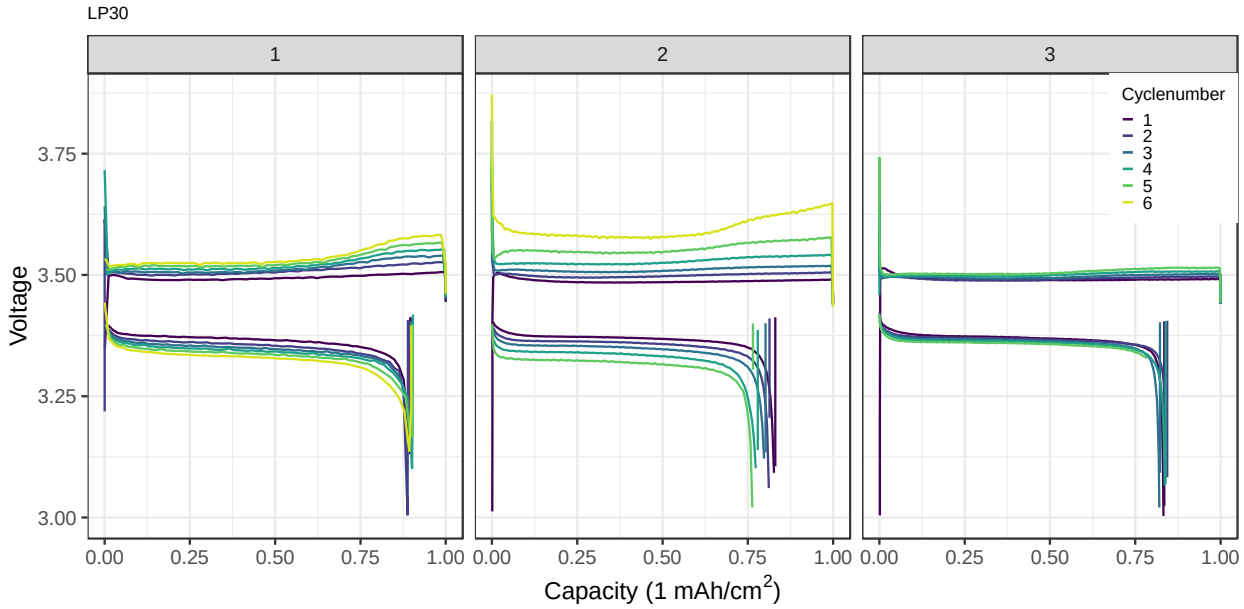

Figure S17. The galvanostatic cycling of Cu-LFP for the three different *in situ* cells (referred to as 1,2,3) performed in LP30 electrolyte with 0.5 mA/cm^2 current density and 1 mAh/cm^2 capacity.

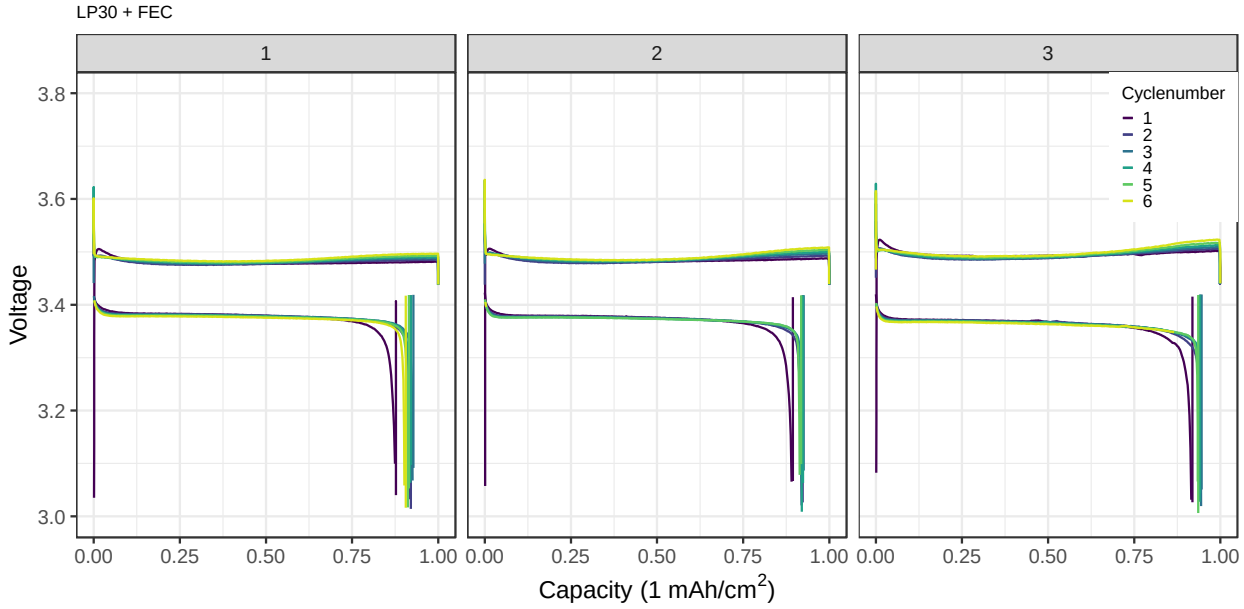

Figure S18. The galvanostatic cycling of Cu-LFP for three different *in situ* cells (referred to as 1,2,3) performed in LP30 + FEC electrolyte with 0.5 mA/cm^2 current density and 1 mAh/cm^2 capacity.

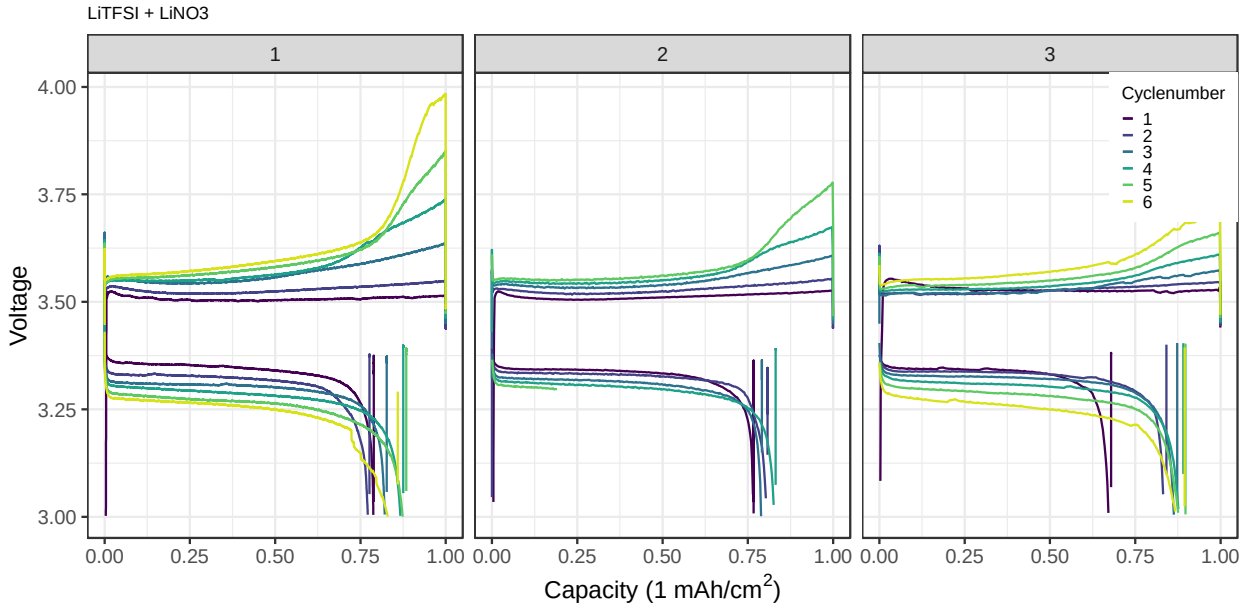

Figure S19. The galvanostatic cycling of Cu-LFP for the three different *in situ* cells (referred to as 1,2,3) performed in 1 M LiTFSI in DOL/DME + 2 wt% $LiNO_3$ electrolyte with 0.5 mA/cm^2 current density and 1 mAh/cm^2 capacity.

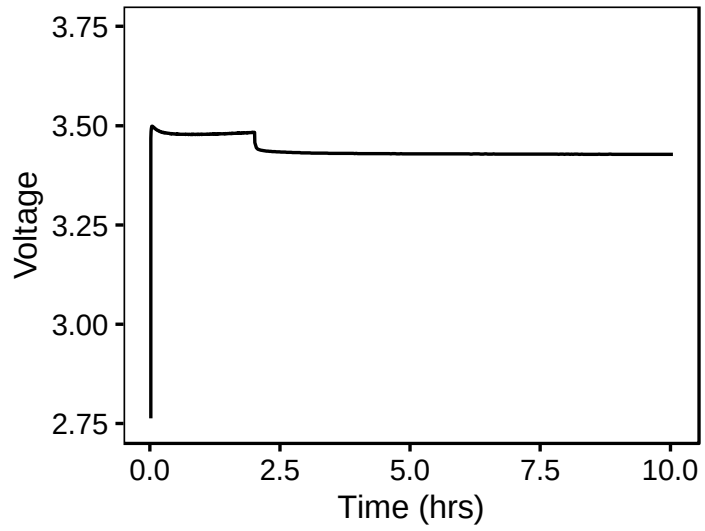

Figure S20. **An example of the electrochemistry for the OCV experiments –** Galvanostatic plating for 2 hours followed with a rest period at the OCV for an *in situ* NMR experiment in LP30 + FEC with 0.5 mA/cm^2 current density

References

(1) Chandrashekar, S.; Trease, N. M.; Chang, H. J.; Du, L.-S. S.; Grey, C. P.; Jerschow, A. 7Li MRI of Li Batteries Reveals Location of Microstructural Lithium. *Nat. Mater.* **2012**, *11* (4), 311–315.

(2) Bhattacharyya, R.; Key, B.; Chen, H.; Best, A. S.; Hollenkamp, A. F.; Grey, C. P. In Situ NMR Observation of the Formation of Metallic Lithium Microstructures in Lithium Batteries. *Nat. Mater.* **2010**, *9* (6), 504–510.

(3) Ilott, A. J.; Chandrashekar, S.; Klöckner, A.; Chang, H. J.; Trease, N. M.; Grey, C. P.; Greengard, L.; Jerschow, A. Visualizing Skin Effects in Conductors with MRI: 7Li MRI Experiments and Calculations. *J. Magn. Reson.* **2014**, *245*, 143–149.

(4) Kittel, C. Introduction to Solid State Physics, 8th Edition. *Wiley Sons, New York, NY* **2004**.

(5) Lide, D. R. *CRC Handbook of Chemistry and Physics, 84th Edition*; CRC: Boca Raton; London, 2003.

(6) Mohammadi, M.; Jerschow, A. In Situ and Operando Magnetic Resonance Imaging of Electrochemical Cells: A Perspective. *J. Magn. Reson.* **2019**, *308*, 106600.

(7) Zhou, L.; Leskes, M.; Ilott, A. J.; Trease, N. M.; Grey, C. P. Paramagnetic Electrodes and Bulk Magnetic Susceptibility Effects in the in Situ NMR Studies of Batteries: Application to Li1.08Mn1.92O4spinels. *J. Magn. Reson.* **2013**, *234*, 44–57.

(8) Schenck, J. F. The Role of Magnetic Susceptibility in Magnetic Resonance Imaging: MRI Magnetic Compatibility of the First and Second Kinds. *Med. Phys.* **1996**, *23* (6), 815–850.

(9) Salomir, R.; De Senneville, B. D.; Moonen, C. T. W. A Fast Calculation Method for Magnetic Field Inhomogeneity Due to an Arbitrary Distribution of Bulk Susceptibility. *Concepts Magn. Reson. Part B Magn. Reson. Eng.* **2003**, *19* (1), 26–34.

(10) Marques, J. P.; Bowtell, R. Application of a Fourier-Based Method for Rapid Calculation of Field Inhomogeneity Due to Spatial Variation of Magnetic Susceptibility. *Concepts Magn. Reson. Part B Magn. Reson. Eng.* **2005**, *25* (1), 65–78.

(11) Chang, H. J.; Trease, N. M.; Ilott, A. J.; Zeng, D.; Du, L. S.; Jerschow, A.; Grey, C. P. Investigating Li Microstructure Formation on Li Anodes for Lithium Batteries by in Situ ^{6}Li/^{7}Li NMR and SEM. *J. Phys. Chem. C* **2015**, *119* (29), 16443–16451.

(12) Rowland, T. J. Nuclear Magnetic Resonance in Metals. *Prog. Mater. Sci.* **1961**, *9* (1), 3–91.

(13) Chang, H. J.; Ilott, A. J.; Trease, N. M.; Mohammadi, M.; Jerschow, A.; Grey, C. P. Correlating Microstructural Lithium Metal Growth with Electrolyte Salt Depletion in Lithium Batteries Using 7Li MRI. *J. Am. Chem. Soc.* **2015**, *137* (48), 15209–15216.

(14) Lopez, J.; Pei, A.; Oh, J. Y.; Wang, G.-J. J. N.; Cui, Y.; Bao, Z. Effects of Polymer Coatings on Electrodeposited Lithium Metal. *J. Am. Chem. Soc.* **2018**, *140* (37), 11735–11744.